RSC
Mechanochemistry

PAPER

View Article Online
View Journal | View Issue

Check for updates

Cite this: *RSC Mechanochem.*, 2026, 3, 106

Mechanochemical synthesis of Ba-doped BiCuSeO oxyselenides: influence of processing conditions on phase formation

Aleksandra Khanina,* Tatyana Sviridova, Alexandra Ivanova, Andrey Voronin and Vladimir Khovaylo*

Received 26th April 2025
Accepted 3rd October 2025

DOI: 10.1039/d5mr00056d

rsc.li/RSCMechanochem

We report a novel rapid synthesis method for Ba-doped BiCuSeO using mechanochemical synthesis. The phase formation mechanism during high-energy milling as well as the combined effects of the powder-to-ball mass ratio and the heterovalent substitution of bismuth by barium on the thermoelectric properties was investigated. It was shown that the single-phase oxyselenide compounds are formed after 25 minutes of ball milling. The thermoelectric properties of these samples were found to be comparable with the properties of oxyselenides prepared *via* conventional solid-state reaction reported in the literature.

Introduction

Every year, interest in alternative energy sources, particularly renewable energy, continues to grow. Among these, thermoelectricity stands out as a promising method for the direct conversion of thermal energy into electrical energy without an intermediate mechanical stage. The efficiency of this conversion is determined by the dimensionless thermoelectric figure of merit, zT, defined as $zT = \alpha^2\sigma T/\kappa_{\text{tot}}$, where α is the Seebeck coefficient, σ is the electrical conductivity, T is the absolute temperature and κ_{tot} is the total thermal conductivity.[1] However, the primary challenge in scaling up thermoelectric energy converters is their relatively low cost-effectiveness in converting waste heat into usable electrical energy. Additionally, to make a meaningful environmental impact, thermoelectric devices must be commercially viable on a much larger scale than their current niche applications. The materials used in these devices must also meet key criteria for scalability, such as the availability and low toxicity of precursors, straightforward synthesis routes, favorable mechanical properties, and high thermal and chemical stability. Even the most well-studied and efficient thermoelectric materials, including skutterudites,[2–4] Heusler alloys,[5,6] zinc and magnesium antimonides,[7,8] as well as tin[9] and copper selenides,[10] silver,[11] and lead tellurides,[12] still fall short in achieving high performance for large-scale thermoelectric applications. A major drawback of these materials is their low thermal and chemical stability when exposed to air.

From this perspective, oxide-based thermoelectric materials, such as zinc oxides,[13,14] perovskites,[15] and oxychalcogenides,[16] offer a significant advantage. Among bismuth-based oxyselenides, BiCuSeO is one of the most promising candidates. BiCuSeO-based compounds have been widely recognized for their exceptionally low thermal conductivity (~0.5–0.9 W m^{-1} K^{-1} at 300 K)[17–21], attributed to their layered structure, the presence of heavy elements, and weak interlayer bonding.[22] However, despite their low thermal conductivity, these materials typically exhibit low charge carrier concentration and mobility. In this regard, the primary approaches towards enhancing thermoelectric properties involve lattice engineering and defect introduction to reduce thermal conductivity, texturing the material to control carrier scattering and optimizing synthesis methods and conditions.[17,23–31] Notably, the intrinsic charge carrier concentration of undoped BiCuSeO is relatively low, approximately 10^{18} cm^{-3}.[19,21,32–37] Therefore, the most common strategy to improve electrical transport is doping at either Bi or Cu sites to increase carrier concentration. Several studies have reported partial substitution with alkaline earth metals such as Mg, Ca, Sr, and Ba,[19,22,38,39] as well as other elements, including Ag, Na, La, Zn, Cd, and S,[29,30,34,40,41,41–44] which have been shown to enhance the thermoelectric performance of oxyselenides in the mid-temperature range. Additionally, Pb doping, often in combination with other elements, has been used to optimize thermoelectric properties.[45–48] It is worth noting that the highest reported zT value for BiCuSeO is 1.6, achieved primarily through shear exfoliation and Pb doping.[49] However, the toxicity of lead has prompted scientists to focus on more environmentally friendly elements such as barium.[19,50–55] Nevertheless, as mentioned earlier, from an industrial perspective, the thermoelectric figure of merit alone is not the sole determining factor for practical application.

Materials and methods

To develop a cost-effective thermoelectric material suitable for large-scale applications, we initiated the scalable production of

---

Academic Research Center for Energy Efficiency, National University of Science and Technology MISIS, Leninsky Av. 4, Moscow, 119049, Russia. E-mail: khanina.as@misis.ru; khovaylo@misis.ru

BiCuSeO oxyselenides using mechanochemical synthesis (MS). MS has long been recognized as an efficient and scalable approach for synthesizing thermoelectric materials, offering a solvent-free, one-step process involving high-energy milling of elemental precursors.[56,57] In contrast, the traditional solid-state reaction (SSR) method involves pre-mixing powder reactants manually or using a ball mill, followed by high-temperature annealing (typically at 773–973 K for 12 hours or more) and intermediate milling in several iterations to ensure homogeneity and complete the reaction.[17–20,33,50–54,58–71] Although both approaches employ solid reactants and often require subsequent consolidation through thermal treatment, MS is fundamentally different in its reaction mechanism: chemical reactions are initiated and sustained by mechanical energy, whereas in SSR, reaction progression is primarily driven by thermal energy. Previous studies have demonstrated that MS can be used to synthesize oxyselenides; however, phase formation typically requires more than 1.5 hours.[23,72–75] Importantly, vacancies play a crucial role in optimizing the thermal and electrical transport properties of oxyselenides.[76] MS is accompanied by the formation of structural defects, including dislocations and point defects (vacancies, interstitials, antisite defects, *etc.*) as well as nanostructuring. These factors can reduce thermal conductivity and enhance thermoelectric performance. In particular, MS promotes the formation of copper vacancies, whose formation energy in BiCuSeO oxyselenides is reported to be close to zero.[77] However, achieving optimal densification after synthesis remains a key challenge. Mechanochemically synthesized materials often require additional compaction steps and tailored consolidation techniques, such as spark plasma sintering or hot pressing, to attain the necessary density and mechanical strength for practical applications.[78] Additionally, potential contamination from the milling medium must be considered, as it may adversely affect material properties. In the context of doping, MS facilitates a uniform distribution of dopants, which is crucial for optimizing electrical conductivity and the Seebeck coefficient. In this work, we demonstrate that barium-doped BiCuSeO oxyselenide can be synthesized from readily available precursors *via* a scalable MS process in just 25 minutes, *i.e.*, much faster than the conventional solid-state reaction (SSR) method, which requires 40 to 70 hours.[33,58]

Oxyselenides with composition $Bi_{1-x}Ba_xCuSeO$ ($x = 0$, 0.075, 0.125 and 0.175) were obtained by mechanochemical synthesis. To facilitate large-scale production of oxyselenide, this study utilizes cost-effective industrial precursors, specifically using copper oxide instead of bismuth oxide. Moreover, as previously reported, employing CuO is thermodynamically more favorable.[79] Accordingly, the commercial high-purity powders of Bi, BaO, Cu, CuO and Se were used as the precursors. A stoichiometric mixture of the raw powders (20 g) was subjected to high-energy ball milling in an air atmosphere using a high-speed planetary ball mill (Activator 2S, Activator, Russia). All samples were milled in 0.25 l steel grinding jars with ∅ 5 mm diameter steel grinding balls. The rotation speed of the jars was 694 rpm, and the grinding time was up to 25 minutes. As previously reported, the phase composition of powders and consequently their transport properties vary with different milling rates or powder-to-ball mass ratios due to differences in the mechanical energy imparted during MS.[80] In order to reveal the influence of mechanical energy applied during milling on the phase formation and resultant thermoelectric performance of BiCuSeO, the powder-to-ball mass ratio was varied from 1 : 10 to 1 : 20 and 1 : 40. The resulting powders were consolidated using the pressureless sintering (PLS) method (Fig. 1). This process involved cold pressing (10 *t*, no holding) into cylindrical tablets (∅ 10.15 mm, 1.5 mm in height), followed by annealing in a sealed quartz ampoule under a 40 kPa argon atmosphere. The annealing was performed at 973 K for 6 hours, with a heating and cooling rate of 1 K min^{-1} down to 473 K, after which the samples were allowed to cool naturally to room temperature. Phase composition analysis was carried out through powder X-ray diffraction (PXRD) using a DRON-4 diffractometer (IC Bourevestnik, Russia) with Co-K$_\alpha$ radiation ($\lambda = 1.79021$ Å) and a Difray-401k desktop diffractometer (SC Scientific Instruments, Russia) with Cr-Kα radiation ($\lambda = 2.2909$ Å). The PXRD patterns were refined by the Rietveld method with the self-developed software package.[81] The uncertainty in the lattice parameters is 0.004 Å for parameter a and 0.009 Å for c, the uncertainty in volume fractions of phases is 5–10%. The fracture morphologies, distribution of the elements and actual chemical composition of all the samples were analyzed by scanning electron microscopy (SEM; Vega 3 SB, Tescan, Czech Republic) equipped with an energy dispersive X-ray spectrometer (EDS; x-act, Oxford Instruments, UK). Additionally, the average particle size of the powders was determined by dynamic light scattering (DLS; Zetasizer Nano ZS, Malvern Panalytical, UK). Consolidated specimens were cut into discs with ∅ 10 and 1.5 mm thickness for the thermal diffusivity measurements and bars with 10 mm length, 1.5 mm height and 2 mm width for the electrical transport measurements. The Seebeck coefficient α and the electrical conductivity σ were simultaneously measured at 300 K by using a homemade Seebeck coefficient/electrical resistivity measuring system (Cryotel Ltd, Russia). The thermal diffusivity χ was measured by using the laser flash diffusivity method (LFA 457, Netzsch, Germany). The thermal conductivity κ_{tot} was calculated using the equation $\kappa_{tot} = \chi C_p d$ where C_p represents the specific heat capacity, which was calculated using the Debye model. The density d was determined using the Archimedes method. The uncertainty in σ and α was 7%, along with 8% in κ_{tot}. The overall uncertainty in zT was estimated to be less than 20%.

Results and discussion

The first series of experiments were focused on studying phase formation as a function of milling time. The chosen mechanochemical synthesis parameters were as follows: 694 rpm, a powder-to-ball mass ratio of 1 : 40, and an air atmosphere. Fig. 2 shows the PXRD patterns of BiCuSeO samples milled for 15, 20, and 25 minutes. For reference, the manually mixed stoichiometric precursor mixture is designated as 0 minutes. As reported in the literature,[73,75,77,79] the formation of the BiCuSeO phase during mechanical milling involves the formation and

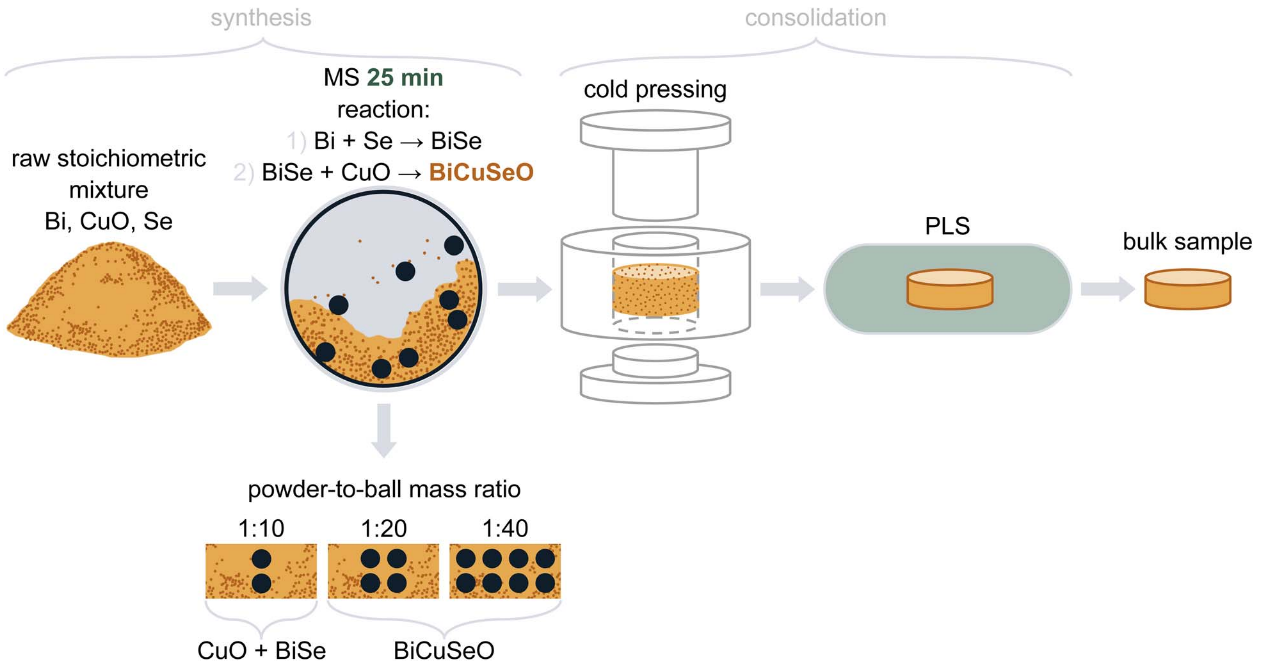

Fig. 1 Schematic representation of the synthesis stages, corresponding reaction products, and consolidation process.

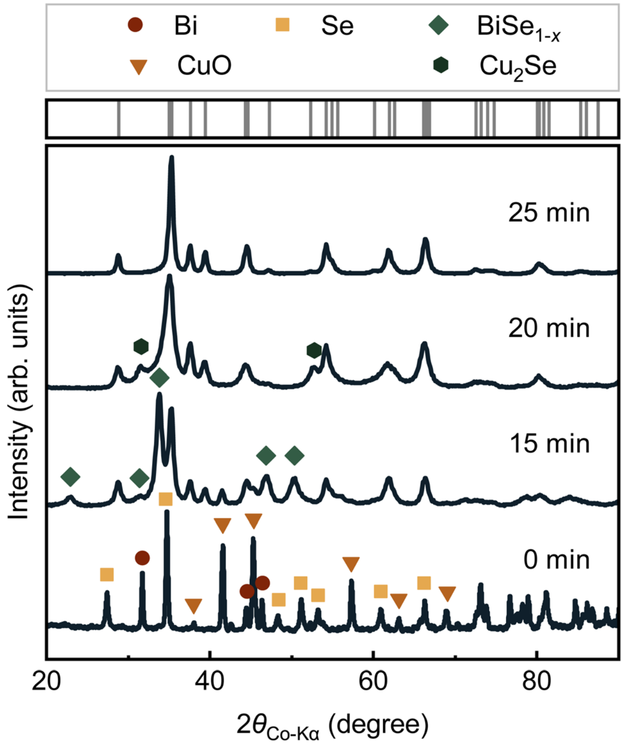

Fig. 2 Powder XRD pattern evolution for the starting mixture of the raw materials with nominal composition of BiCuSeO at a powder-to-ball mass ratio of 1 : 40 and increasing milling time. Bragg's reflections for the BiCuSeO phase are indicated by gray ticks on the top part of the figure.

subsequent reaction of intermediate phases, including bismuth selenides and copper oxide. After 15 minutes of milling, the powder consists of an intermediate phase $BiSe_{1-x}$ (45 wt%), the target BiCuSeO phase (40 wt%) and unreacted CuO (15 wt%). Extending the milling time to 20 minutes significantly increases the content of the BiCuSeO phase to 85 wt%, and appearance of an intermediate phase, Cu_2Se, whose content is 15 wt%. After 25 minutes of milling, the phase formation is complete, and reflections only from the BiCuSeO phase are observed on the PXRD patterns (Fig. 2). All major reflections can be attributed to the tetragonal BiCuSeO phase (PDF#01-076-6689) with a ZrCuSiAs structural type and a $P4/mmm$ space group.

Based on the previously described results, a second series of experiments was conducted for 25 min in air to study the effect of the powder-to-ball mass ratio on the formation of the Ba-doped oxyselenide phase. Fig. 3 shows the PXRD patterns of the $Bi_{1-x}Ba_xCuSeO$ (x = 0, 0.075, 0.125, 0.175) samples. The undoped sample, milled at a powder-to-ball mass ratio of 1 : 10, retains significant amounts of unreacted precursors and intermediate phases, specifically $BiSe_{1-x}$ (35 wt%) and CuO (15 wt%). This indicates that the relatively mild milling conditions do not provide sufficient energy to complete the reaction. The results suggest that at this ratio, the amount of secondary phases decreases with increasing Ba concentration. For the sample with $x = 0.075$, only a small amount of unreacted CuO (5 wt%) was detected, while no secondary phases were observed in samples with $x > 0.075$. Similarly, when milling at a ratio of 1 : 40, the undoped sample still contains CuO (5 wt%). Based on these findings, a powder-to-ball mass ratio of 1 : 20 appears to be optimal for the BiCuSeO synthesis. After the PLS process, phase composition changes were observed in almost all samples, with the formation of secondary phases such as $BiSe_{1-x}$, Bi_2O_3, and Cu_2O (Fig. S1). Notably, in powders synthesized at a 1 : 10 powder-to-ball mass ratio, the BiCuSeO phase formation was completed during PLS. This suggests that

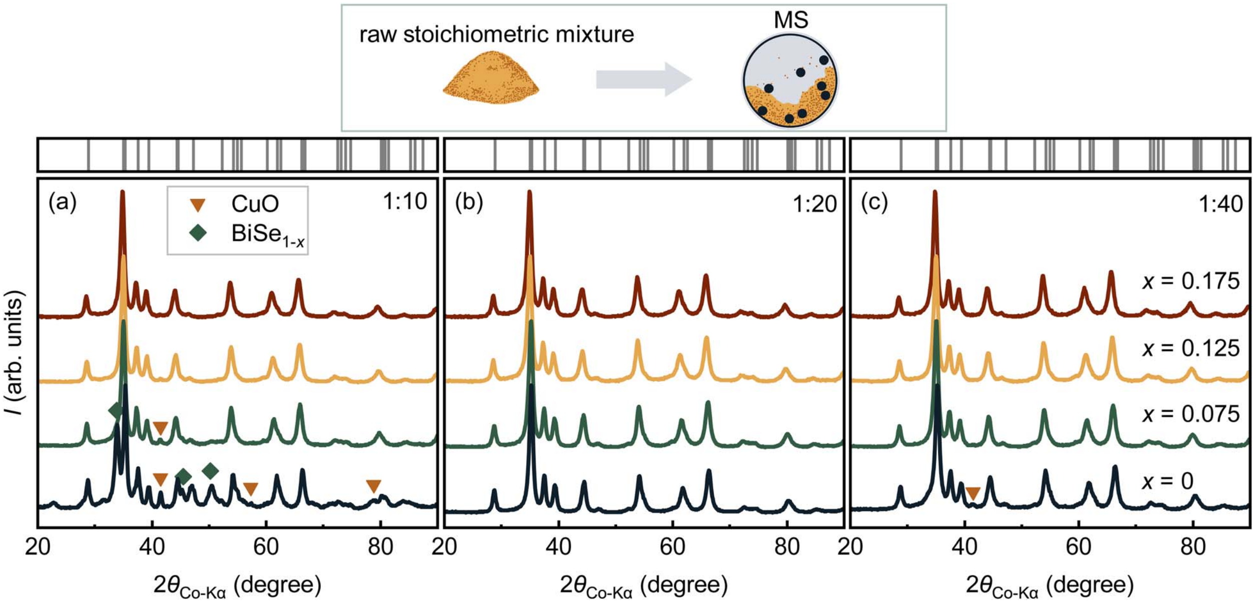

Fig. 3 Powder XRD patterns of the $Bi_{1-x}Ba_xCuSeO$ ($x = 0$, 0.075, 0.125, 0.175) samples after MS with powder-to-ball mass ratios of (a) 1 : 10, (b) 1 : 20, and (c) 1 : 40. Bragg's reflections for the BiCuSeO phase are indicated by gray ticks on the top part of the figure.

to achieve a predominantly BiCuSeO phase, a minimum milling time of 25 minutes at a 1 : 10 ratio and a rotation speed of 694 rpm is required, followed by reaction sintering during the PLS process to ensure complete phase formation.

The refined lattice parameters of BiCuSeO are in good agreement with previously reported values for samples synthesized *via* SSR[34] and MS[79] (see Table S1 and Fig. 4a). When oxyselenide samples are prepared by MS, point defects such as copper vacancies (V_{Cu}) may form.[77] It is important to note that copper vacancies can have a significant impact on the transport properties of oxyselenide.[37,82,83] In this case, two competing factors can influence the evolution of lattice parameters in doped $Bi_{1-x}Ba_xCuSeO$ ($x = 0$, 0.075, 0.125, 0.175) oxyselenides. Copper deficiency tends to decrease the lattice parameters a and c,[17] while doping with Ba^{2+} (1.42 Å), which has a larger ionic radius than bismuth Bi^{3+} (1.17 Å),[55] should lead to an increase in the lattice parameters.[19,51] Our experimental data indicate that doping is the dominant factor, resulting in a gradual linear increase in both lattice parameters a and c (Fig. 4 and Table S1). However, a slight decrease in the lattice parameters is observed with an increase in the powder-to-ball mass ratio, which is likely due to the formation of V_{Cu}.

The Bi : Cu : Se elemental ratio for all compositions deviates slightly from the nominal 1 : 1 : 1 ratio, remaining within the error limits of the EDS method. In most cases, an excess of Bi and a deficiency of Cu are observed (Table S1). However, we propose that this non-stoichiometry is intrinsically linked to the reaction pathway, which proceeds through the formation of copper-deficient intermediate phases such as $BiSe_{1-x}$ and Cu_2Se, as identified by XRD (Fig. 2). The kinetics of this diffusion-controlled solid-state process[84] appear to favor the formation and persistence of these defective intermediates, ultimately leading to the incorporation of copper vacancies (V_{Cu}) into the final BiCuSeO lattice. The measured Ba/(Bi + Ba) ratio closely matches the nominal values, confirming the intended doping levels. The EDS data are also consistent with

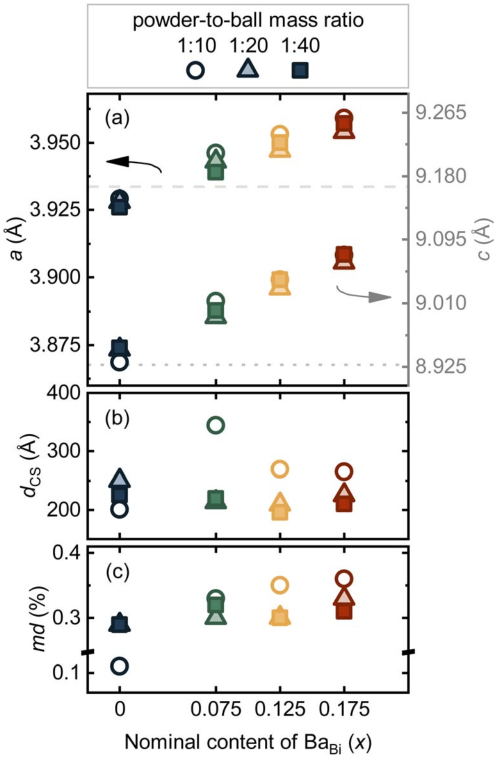

Fig. 4 (a) Lattice parameters a and c (comparative data from Wu *et al.*:[79] dashed line – parameter a and dotted line – parameter c), (b) crystallite size d_{CS} and (c) microdeformation (md) as a function of nominal Ba_{Bi} concentration.

the PXRD results, confirming the presence of CuO and $BiSe_{1-x}$ inclusions in the samples milled at a powder-to-ball mass ratio of 1 : 10 (Fig. 5 and S3). The values of the crystallite size (d_{CS}) systematically decrease with increasing powder-to-ball mass ratio, which is explained by the higher milling energies (Fig. 4b and Table S1). However, Ba substitution does not introduce significant changes, and the CS values remain in a similar range without exhibiting a clear monotonic trend. The impact of the powder-to-ball mass ratio on reaction kinetics can be explained in terms of stress-induced electron redistribution at interfaces of dissimilar solids. Our precursor mixture is a complex interface of metals, a semiconductor, and insulators. During high-energy ball milling, these interfaces experience extreme mechanical stress, which is quantitatively evidenced by the microdeformations (md). As shown in Fig. 4c, the systematic increase in microdeformation values with higher barium content is attributed to the larger ionic radius of Ba^{2+}, which induces significant local lattice distortion and amplifies the internal stress fields. According to the model proposed by Sun *et al.*,[85] the stress does not merely create fresh surfaces and defects; it directly modifies the electronic states at the interfaces, leading to significant charge redistribution (*e.g.*, from metallic Bi/Cu to CuO). The powder-to-ball mass ratio is a direct control parameter for this process: a higher ratio increases the frequency and force of these triboelectrically active collisions, thereby amplifying the cumulative charge redistribution effect. At the same time, the high microstrain values for the 1 : 10 ratio, particularly in the doped samples, are interpreted as a consequence of incomplete reaction and the persistence of hard, unreacted precursor phases, which create localized stress and hinder homogeneous plastic deformation. Thus, increased mechanical energy input efficiently drives the diffusion-controlled synthesis of complex oxyselenides, far surpassing what thermal energy alone could achieve under similar conditions.

The microstructure of oxyselenides strongly depends on the synthesis method. MS produces fine powders with average particle sizes of approximately 189, 143, and 89 nm for the powders milled at 1 : 10, 1 : 20, and 1 : 40 ratios, respectively (Fig. S2). These values are significantly smaller than those observed in samples synthesized *via* conventional SSR methods.[19,51,54,60–63,65,86] Moreover, MS promotes particle dispersion and introduces numerous defects and microstrains, leading to an increased grain boundary area. This, in turn, enhances phonon scattering and effectively reduces thermal conductivity. After 6 hours of PLS, the grain and agglomerate sizes consistently increase to 5–10 μm for all ratios. However, the density of the resulting volumetric images remains relatively low, ranging from 79% to 88%. Thus, all samples exhibit fine grains with a lath morphology, randomly oriented, which results from the high polycrystallinity of the material (Fig. S4).

For all samples, the Seebeck coefficient values are positive, indicating p-type conductivity. The absolute values range from 80 to 250 $\mu V\ K^{-1}$ at room temperature (Fig. 6a and b). An increase in the Ba_{Bi} concentration and the powder-to-ball mass ratio leads to a decrease in α at 300 K, likely due to a higher charge carrier concentration.[1] However, for undoped compositions, the α values are slightly lower than those reported in the literature,[19,51,52,75,87] which may be attributed to a higher charge carrier concentration resulting from copper vacancies formed during MS.

The electrical conductivity σ exhibits an inverse dependence on concentration across all compositions, gradually increasing with the increasing concentration of barium substituting for bismuth (Fig. 6c and d). Notably, for each powder-to-ball mass ratio, the undoped samples demonstrate higher σ values than those reported in previous studies on oxyselenides synthesized *via* MS, self-propagating high-temperature synthesis, sol–gel, microwave, and SSR.[19,23,51–53,61,64,68,75,88–91] This observation suggests a high carrier concentration, likely due to V_{Cu}. Increasing the powder-to-ball mass ratio to 1 : 20 naturally enhances σ, whereas a further increase to 1 : 40 results in a slight decrease in the absolute σ values, presumably due to an increased defect density and, consequently, enhanced charge carrier scattering. However, a different trend is observed for the sample with $x = 0.075$, where the highest σ value corresponds to the composition milled at a 1 : 40 ratio. For the remaining samples, the highest σ values are achieved at a powder-to-ball mass ratio of 1 : 20. The highest absolute σ values, approximately 350 $\Omega^{-1}\ cm^{-1}$ at 300 K, are obtained for the sample with

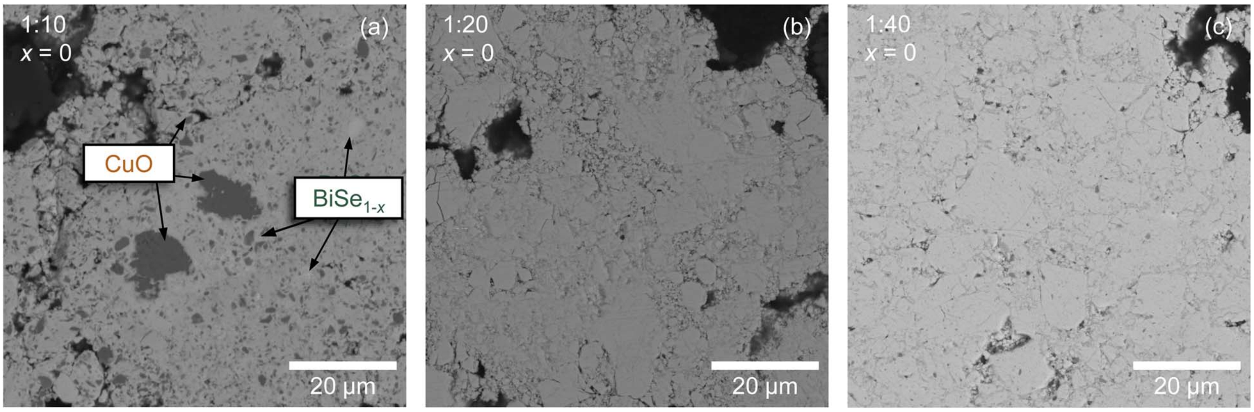

Fig. 5 SEM micrograph of the polished surface of the BiCuSeO samples obtained with powder-to-ball mass ratios of (a) 1 : 10, (b) 1 : 20, and (c) 1 : 40.

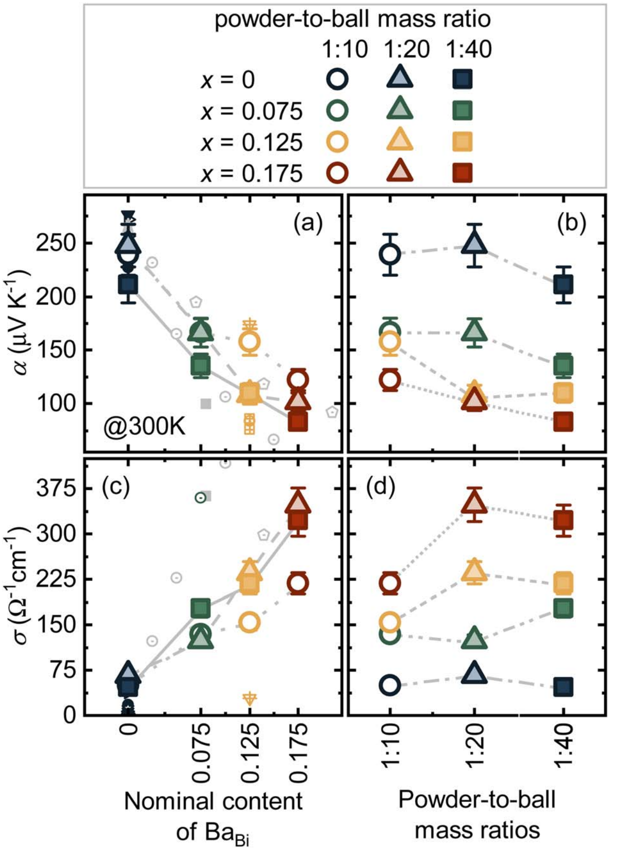

Fig. 6 Concentration and powder-to-ball mass ratio dependence of the (a and b) Seebeck coefficient α and (c and d) electrical conductivity σ for $Bi_{1-x}Ba_xCuSeO$ ($x = 0$, 0.075, 0.125, 0.175) samples consolidated by PLS. Literature data for other $Bi_{1-x}Ba_xCuSeO$-based oxyselenides are also shown for comparison (Feng *et al.*,[75] Li *et al.*,[19] Park *et al.*,[51] Pei *et al.*,[52] Jiang *et al.*,[88] Kim *et al.*,[61] Lei *et al.*,[89] Liang *et al.*,[64] Liu *et al.*,[90] Pan *et al.*,[68] Park *et al.*,[51] Wen *et al.*,[53] Yang *et al.*,[91] Zeng *et al.*,[23] Li *et al.*,[86] and Yang *et al.*[54]). All displayed data points correspond to values obtained at 300 K.

the highest dopant concentration, $Bi_{0.825}Ba_{0.175}CuSeO$, milled at a 1 : 20 ratio. However, the absolute conductivity values for the Ba-doped samples remain lower than those reported for as-synthesized SSR composites in the literature,[51,53,54,86] likely due to the MS process, which introduces numerous additional scattering centers, including grain boundaries, dislocations, and point defects.

The total thermal conductivity κ_{tot} for all samples is approximately 0.7–0.9 W m^{-1} K^{-1} at 300 K, which is in good agreement with Feng *et al.*'s results for MS oxyselenides (Fig. S5a and b).[75] Thermal measurements indicate that barium doping leads to an increase in κ_{tot}, which can be understood by considering electron (κ_{el}) and lattice (κ_{lat}) components of κ_{tot}. The electron thermal conductivity κ_{el} is proportional to the electrical conductivity, σ, following the Wiedemann–Franz law: $\kappa_{el} = \sigma LT$. Here, the Lorentz number, L, was temperature-dependent and estimated using experimental values of the Seebeck coefficient in the framework of the effective mass model. The primary reason for the observed increase in κ_{tot} is the rise in κ_{el}, which directly correlates with σ due to a higher charge carrier concentration (Fig. S5e and f). Comparison of the lattice component of thermal conductivity with literature data suggests that structural defects, including pores—whose formation was promoted by the MS process—introduce additional phonon scattering surfaces, thereby reducing their mean free path (Fig. S5c and d). Additionally, the low density of bulk samples contributes to a decrease in the speed of sound within the material, which is proportional to κ_{lat}.

Based on the measured electrical and thermal transport characteristics, the thermoelectric figure of merit, zT, was calculated and is presented as a function of temperature in Fig. 6g and h. Although the zT values exhibit only minor variations within the error range for different powder-to-ball mass ratios, it is noteworthy that the highest thermoelectric figure of merit for all compositions was achieved for the samples milled at a ratio of 1 : 10. While the obtained zT values are not the highest reported for Ba-doped oxyselenides, they fall within the range of 0.07 to 0.13 at $T = 300$ K, consistent with previously published results. Moreover, the zT values obtained for undoped compositions are higher (about 0.1 at 300 K) than those reported for finely dispersed BiCuSeO powders prepared *via* sol–gel or ball milling methods,[23,75,90,92] as well as for BiCuSeO synthesized by more established techniques such as self-propagating high-temperature synthesis, microwave-assisted synthesis, and SSR.[51–53,61,64,86,88,89,91] This confirms that mechanochemical synthesis, requiring only 25 minutes, is a promising approach for the large-scale production of $Bi_{1-x}Ba_xCuSeO$-based oxyselenides.

Conclusions

In this work, Ba-doped BiCuSeO oxyselenide samples were successfully prepared *via* mechanochemical synthesis followed by pressureless sintering. It was demonstrated that the single-phase oxyselenide powders can be synthesized in just 25 minutes—significantly faster than traditional solid-phase synthesis methods, which require tens of hours. Notably, all stages (except compaction) can be performed in air at room temperature, enabling the synthesis of large powder volumes. The Ba-doped BiCuSeO exhibited zT values of 0.07–0.13, while undoped BiCuSeO achieved even higher zT values than oxyselenides produced by well-established methods such as self-propagating high-temperature synthesis, sol–gel, microwave-assisted synthesis, and solid-state reaction at room temperature. These results confirm the efficiency of the proposed synthesis method, which combines rapid material production with the retention of key thermoelectric properties. These findings open avenues for further optimization of the material's composition and microstructure to enhance thermoelectric performance, as well as for its practical application in energy conversion devices.

Author contributions

Aleksandra Khanina: investigation, conceptualization, methodology, formal analysis, visualization, writing – original draft, writing – review & editing; Tatyana Sviridova: investigation,

formal analysis; Aleksandra Ivanova: investigation; Andrey Voronin: resources; Vladimir Khovaylo: resources, supervision, writing – review & editing.

Conflicts of interest

There are no conflicts to declare.

Data availability

The data supporting this article have been included as part of the supplementary information (SI). Supplementary information is available. See DOI: **https://doi.org/10.1039/d5mr00056d**.

Acknowledgements

The study was carried out with financial support from the Russian Science Foundation, project No. 19-79-10282. A. Khanina is very grateful to A. Novitskii and I. Serhiienko from the National Institute for Materials Science (Japan) for their invaluable assistance in the experimental work, fruitful discussions, and constructive contributions to the conceptualization of this research.

References

1 A. F. Ioffe, *Semiconductor Thermoelements, and Thermoelectric Cooling, Infosearch*, 1957.
2 Y. Tang, S.-w. Chen and G. J. Snyder, *J. Materiomics*, 2015, **1**, 75–84.
3 G. Rogl and P. Rogl, *Curr. Opin. Green Sustainable Chem.*, 2017, **4**, 50–57.
4 A. Ivanova, A. Novitskii, I. Serhiienko, G. Guélou, T. Sviridova, S. Novikov, M. Gorshenkov, A. Bogach, A. Korotitskiy, A. Voronin, *et al.*, *J. Mater. Chem. A*, 2023, **11**, 2334–2342.
5 M. Gürth, G. Rogl, V. Romaka, A. Grytsiv, E. Bauer and P. Rogl, *Acta Mater.*, 2016, **104**, 210–222.
6 G. Rogl, P. Sauerschnig, Z. Rykavets, V. Romaka, P. Heinrich, B. Hinterleitner, A. Grytsiv, E. Bauer and P. Rogl, *Acta Mater.*, 2017, **131**, 336–348.
7 Y. Sun, M. Christensen, S. Johnsen, N. V. Nong, Y. Ma, M. Sillassen, E. Zhang, A. E. Palmqvist, J. Bøttiger and B. B. Iversen, *Adv. Mater.*, 2012, **24**, 1693–1696.
8 L. Wang, W. Zhang, S. Y. Back, N. Kawamoto, D. H. Nguyen and T. Mori, *Nat. Commun.*, 2024, **15**, 6800.
9 C. Zhou, Y. K. Lee, Y. Yu, S. Byun, Z.-Z. Luo, H. Lee, B. Ge, Y.-L. Lee, X. Chen, J. Y. Lee, *et al.*, *Nat. Mater.*, 2021, **20**, 1378–1384.
10 H. Hu, Y. Ju, J. Yu, Z. Wang, J. Pei, H.-C. Thong, J.-W. Li, B. Cai, F. Liu, Z. Han, *et al.*, *Nat. Mater.*, 2024, **23**, 527–534.
11 J. A. Perez-Taborda, O. Caballero-Calero, L. Vera-Londono, F. Briones and M. Martin-Gonzalez, *Adv. Energy Mater.*, 2018, **8**, 1702024.
12 K. Biswas, J. He, Q. Zhang, G. Wang, C. Uher, V. P. Dravid and M. G. Kanatzidis, *Nat. Chem.*, 2011, **3**, 160–166.
13 P. Jood, R. J. Mehta, Y. Zhang, G. Peleckis, X. Wang, R. W. Siegel, T. Borca-Tasciuc, S. X. Dou and G. Ramanath, *Nano Lett.*, 2011, **11**, 4337–4342.
14 I. Serhiienko, A. Novitskii, F. Garmroudi, E. Kolesnikov, E. Chernyshova, T. Sviridova, A. Bogach, A. Voronin, H. D. Nguyen, N. Kawamoto, *et al.*, *Adv. Sci.*, 2024, 2309291.
15 H. Muta, K. Kurosaki and S. Yamanaka, *J. Alloys Compd.*, 2003, **350**, 292–295.
16 S. Tippireddy, P. K. DS, S. Das and R. C. Mallik, *ACS Appl. Energy Mater.*, 2021, **4**, 2022–2040.
17 Y. Liu, L.-D. Zhao, Y. Liu, J. Lan, W. Xu, F. Li, B.-P. Zhang, D. Berardan, N. Dragoe, Y.-H. Lin, *et al.*, *J. Am. Chem. Soc.*, 2011, **133**, 20112–20115.
18 F. Li, J.-F. Li, L.-D. Zhao, K. Xiang, Y. Liu, B.-P. Zhang, Y.-H. Lin, C.-W. Nan and H.-M. Zhu, *Energy Environ. Sci.*, 2012, **5**, 7188–7195.
19 J. Li, J. Sui, Y. Pei, C. Barreteau, D. Berardan, N. Dragoe, W. Cai, J. He and L.-D. Zhao, *Energy Environ. Sci.*, 2012, **5**, 8543–8547.
20 J.-L. Lan, Y.-C. Liu, B. Zhan, Y.-H. Lin, B. Zhang, X. Yuan, W. Zhang, W. Xu and C.-W. Nan, *Adv. Mater.*, 2013, **25**, 5086–5090.
21 Y.-L. Pei, J. He, J.-F. Li, F. Li, Q. Liu, W. Pan, C. Barreteau, D. Berardan, N. Dragoe and L.-D. Zhao, *NPG Asia Mater.*, 2013, **5**, e47.
22 L. Zhao, D. Berardan, Y. Pei, C. Byl, L. Pinsard-Gaudart and N. Dragoe, *Appl. Phys. Lett.*, 2010, **97**, 092118.
23 X. Zeng, Z. Ma, W. Li, B. Yang, Y. Qian, Y. Luo, J. Yang, Y. Liu and Q. Jiang, *Chem. Eng. J.*, 2023, **474**, 145663.
24 Z. Li, C. Xiao, S. Fan, Y. Deng, W. Zhang, B. Ye and Y. Xie, *J. Am. Chem. Soc.*, 2015, **137**, 6587–6593.
25 H. Hiramatsu, H. Yanagi, T. Kamiya, K. Ueda, M. Hirano and H. Hosono, *Chem. Mater.*, 2008, **20**, 326–334.
26 L. Pan, Y. Lang, L. Zhao, D. Berardan, E. Amzallag, C. Xu, Y. Gu, C. Chen, L.-D. Zhao, X. Shen, *et al.*, *J. Mater. Chem. A*, 2018, **6**, 13340–13349.
27 B. Feng, G. Li, Y. Hou, C. Zhang, C. Jiang, J. Hu, Q. Xiang, Y. Li, Z. He, *et al.*, *J. Alloys Compd.*, 2017, **712**, 386–393.
28 G.-K. Ren, S.-Y. Wang, Y.-C. Zhu, K. J. Ventura, X. Tan, W. Xu, Y.-H. Lin, J. Yang and C.-W. Nan, *Energy Environ. Sci.*, 2017, **10**, 1590–1599.
29 Y. Liu, J. Ding, B. Xu, J. Lan, Y. Zheng, B. Zhan, B. Zhang, Y. Lin and C. Nan, *Appl. Phys. Lett.*, 2015, **106**, 233903.
30 Y.-c. Liu, Y.-h. Zheng, B. Zhan, K. Chen, S. Butt, B. Zhang and Y.-h. Lin, *J. Eur. Ceram. Soc.*, 2015, **35**, 845–849.
31 J. Sui, J. Li, J. He, Y.-L. Pei, D. Berardan, H. Wu, N. Dragoe, W. Cai and L.-D. Zhao, *Energy Environ. Sci.*, 2013, **6**, 2916–2920.
32 Y. Liu, L.-D. Zhao, Y. Zhu, Y. Liu, F. Li, M. Yu, D.-B. Liu, W. Xu, Y.-H. Lin and C.-W. Nan, *Adv. Energy Mater.*, 2016, **6**, 1502423.
33 C. Barreteau, D. Bérardan, E. Amzallag, L. Zhao and N. Dragoe, *Chem. Mater.*, 2012, **24**, 3168–3178.
34 J. Li, J. Sui, Y. Pei, X. Meng, D. Berardan, N. Dragoe, W. Cai and L.-D. Zhao, *J. Mater. Chem. A*, 2014, **2**, 4903–4906.
35 M. Ishizawa, Y. Yasuzato, H. Fujishiro, T. Naito, H. Katsui and T. Goto, *J. Appl. Phys.*, 2018, **123**, 245104.

36 Y. Sun, C. Zhang, C. Cao, J. Fu and L. Peng, *Ceram. Int.*, 2017, **43**, 17186–17193.

37 L.-D. Zhao, J. He, D. Berardan, Y. Lin, J.-F. Li, C.-W. Nan and N. Dragoe, *Energy Environ. Sci.*, 2014, **7**, 2900–2924.

38 J. Li, J. Sui, C. Barreteau, D. Berardan, N. Dragoe, W. Cai, Y. Pei and L.-D. Zhao, *J. Alloys Compd.*, 2013, **551**, 649–653.

39 F. Li, T.-R. Wei, F. Kang and J.-F. Li, *J. Mater. Chem. A*, 2013, **1**, 11942–11949.

40 S. Tan, H. Lei, D. Shao, H. Lv, W. Lu, Y. Huang, Y. Liu, B. Yuan, L. Zu, X. Kan, *et al.*, *Appl. Phys. Lett.*, 2014, **105**, 082109.

41 M. Farooq, S. Butt, K. Gao, Y. Zhu, X. Sun, X. Pang, S. U. Khan, F. Mohmed, A. Mahmood, N. Mahmood, *et al.*, *RSC Adv.*, 2016, **6**, 33789–33797.

42 G. Ren, S. Butt, C. Zeng, Y. Liu, B. Zhan, J. Lan, Y. Lin and C. Nan, *J. Electron. Mater.*, 2015, **44**, 1627–1631.

43 M.-K. Han, Y.-S. Jin, B. K. Yu, W. Choi, T.-S. You and S.-J. Kim, *J. Mater. Chem. A*, 2016, **4**, 13859–13865.

44 M. Zhang, J. Yang, Q. Jiang, L. Fu, Y. Xiao, Y. Luo, D. Zhang, Y. Cheng and Z. Zhou, *J. Electron. Mater.*, 2015, **44**, 2849–2855.

45 B. Feng, G. Li, Z. Pan, X. Hu, P. Liu, Z. He, Y. Li, *et al.*, *J. Solid State Chem.*, 2019, **271**, 1–7.

46 A. Khanina, A. Novitskii, D. Pashkova, A. Voronin, T. Mori and V. Khovaylo, *Phys. Chem. Chem. Phys.*, 2024, **26**, 13006–13011.

47 J. Qiu, Y. Lei, F. Gao, Y. Li, L. Tao, C. Yong and H. Hu, *Inorg. Chem.*, 2022, **62**, 353–362.

48 S. Das, S. M. Valiyaveettil, K.-H. Chen, S. Suwas and R. Chandra Mallik, *AIP Adv.*, 2019, **9**, 015025.

49 Y. Gu, X.-L. Shi, L. Pan, W.-D. Liu, Q. Sun, X. Tang, L.-Z. Kou, Q.-F. Liu, Y.-F. Wang and Z.-G. Chen, *Adv. Funct. Mater.*, 2021, **31**, 2101289.

50 D. Feng, F. Zheng, D. Wu, M. Wu, W. Li, L. Huang, L.-D. Zhao and J. He, *Nano Energy*, 2016, **27**, 167–174.

51 K. Park, D. Kim, H. Hong, G. Jung and J. Pi, *Ceram. Int.*, 2019, **45**, 9604–9610.

52 Y.-L. Pei, H. Wu, D. Wu, F. Zheng and J. He, *J. Am. Chem. Soc.*, 2014, **136**, 13902–13908.

53 Q. Wen, H. Zhang, F. Xu, L. Liu, Z. Wang and G. Tang, *J. Alloys Compd.*, 2017, **711**, 434–439.

54 T.-Y. Yang, L. Huang, J. Guo, Y. Zhang, J. Feng and Z.-H. Ge, *ACS Appl. Energy Mater.*, 2021, **4**, 13077–13084.

55 D. Yuan, S. Guo, S. Hou, Y. Ma, J. Wang and S. Wang, *Nanoscale Res. Lett.*, 2018, **13**, 1–9.

56 W. H. Nam, E.-J. Meang, Y. S. Lim, S. Lee, W.-S. Seo and J. Y. Lee, *J. Electr. Electron. Mater.*, 2015, **28**, 852–856.

57 H. J. Im, B. Koo, M.-S. Kim and J. E. Lee, *Korean J. Chem. Eng.*, 2022, **39**, 1227–1231.

58 Y.-X. Chen, W. Qin, A. Mansoor, A. Abbas, F. Li, G.-x. Liang, P. Fan, M. U. Muzaffar, B. Jabar, Z.-h. Ge, *et al.*, *Nano Res.*, 2023, **16**, 1679–1687.

59 S. Das, R. Chetty, K. Wojciechowski, S. Suwas and R. C. Mallik, *Appl. Surf. Sci.*, 2017, **418**, 238–245.

60 H. Hong, D. Kim and K. Park, *Ceram. Int.*, 2022, **48**, 19618–19625.

61 D. Kim, H. Hong and K. Park, *J. Alloys Compd.*, 2021, **876**, 159969.

62 F. Li, Z. Zheng, Y. Chang, M. Ruan, Z. Ge, Y. Chen and P. Fan, *ACS Appl. Mater. Interfaces*, 2019, **11**, 45737–45745.

63 F. Li, M. Ruan, Y. Chen, W. Wang, J. Luo, Z. Zheng and P. Fan, *Inorg. Chem. Front.*, 2019, **6**, 799–807.

64 X. Liang, R. Xu, M. Kong, H. Wan, W. Bai, D. Dong, Q. Li, H. Xu, Z. Li, B. Ge, *et al.*, *Mater. Today Phys.*, 2023, **34**, 101084.

65 Y. Liu, Y. Zhu, W.-S. Liu, A. Marcelli and W. Xu, *J. Am. Ceram. Soc.*, 2019, **102**, 1541–1547.

66 S. D. Luu and P. Vaqueiro, *J. Mater. Chem. A*, 2013, **1**, 12270–12275.

67 N. Madhukar, K. Gurukrishna, B. R. Bhat, U. D. Shanubhogue, S. Mangavati, A. Rao and S. Chattopadhyay, *Appl. Phys. A:Mater. Sci. Process.*, 2024, **130**, 55.

68 L. Pan, D. Bérardan, L. Zhao, C. Barreteau and N. Dragoe, *Appl. Phys. Lett.*, 2013, **102**, 023902.

69 Q. Wen, C. Chang, L. Pan, X. Li, T. Yang, H. Guo, Z. Wang, J. Zhang, F. Xu, Z. Zhang, *et al.*, *J. Mater. Chem. A*, 2017, **5**, 13392–13399.

70 R. Xu, Z. Chen, Q. Li, X. Yang, H. Wan, M. Kong, W. Bai, N. Zhu, R. Wang, J. Song, *et al.*, *Research*, 2023, **6**, 0123.

71 H. Zhu, Z. Li, C. Zhao, X. Li, J. Yang, C. Xiao and Y. Xie, *Natl. Sci. Rev.*, 2021, **8**, nwaa085.

72 V. Pele, C. Barreteau, D. Berardan, L. Zhao and N. Dragoe, *J. Solid State Chem.*, 2013, **203**, 187–191.

73 A. Novitskii, I. Serhiienko, E. Kolesnikov, E. Zakharova, A. Voronin and V. Khovaylo, *Mater. Lett.*, 2020, **262**, 127184.

74 Z. Pei, G. Xiang, X. Sun, Z. Fu, Y. Qiao, L. Wang, S. Dong and J. Chen, *Coatings*, 2023, **13**, 2069.

75 B. Feng, G. Li, Z. Pan, H. Xiaoming, L. Peihai, H. Zhu, L. Yawei, *et al.*, *J. Alloys Compd.*, 2018, **754**, 131–138.

76 P. Vaqueiro, R. A. R. Al Orabi, S. D. Luu, G. Guelou, A. V. Powell, R. Smith, J.-P. Song, D. Wee and M. Fornari, *Phys. Chem. Chem. Phys.*, 2015, **17**, 31735–31740.

77 M. Y. Toriyama, J. Qu, G. J. Snyder and P. Gorai, *J. Mater. Chem. A*, 2021, **9**, 20685–20694.

78 I. O. Tampubolon, P. Jacko, M. Bereš, P. Baláž and M. Baláž, *J. Vis. Exp.*, 2024, e67249.

79 J. Wu, F. Li, T.-R. Wei, Z. Ge, F. Kang, J. He and J.-F. Li, *J. Am. Ceram. Soc.*, 2016, **99**, 507–514.

80 C. Suryanarayana, *Prog. Mater. Sci.*, 2001, **46**, 1–184.

81 E. Shelekhov and T. Sviridova, *Met. Sci. Heat Treat.*, 2000, **42**, 309–313.

82 D. Kim, H. Hong, J. Lee, S. Park and K. Park, *J. Mater. Res. Technol.*, 2020, **9**, 16202–16213.

83 W. Xu, Y. Liu, L.-D. Zhao, P. An, Y.-H. Lin, A. Marcelli and Z. Wu, *J. Mater. Chem. A*, 2013, **1**, 12154–12158.

84 J. Li, G. Liu, X. Wu, G. He, Z. Yang and J. Li, *Ceram. Int.*, 2018, **44**, 22172–22175.

85 J. Sun, Y. Jiang, S. Du, L. Chen, J. S. Francisco, S. Cui, Q. Huang and L. Qian, *Nano Lett.*, 2024, **24**, 6858–6864.

86 F. Li, J.-F. Li, L.-D. Zhao, K. Xiang, Y. Liu, B.-P. Zhang, Y.-H. Lin, C.-W. Nan and H.-M. Zhu, *Energy Environ. Sci.*, 2012, **5**, 7188–7195.

87 A. Novitskii, I. Serhiienko, S. Novikov, K. Kuskov, D. Pankratova, T. Sviridova, A. Voronin, A. Bogach, E. Skryleva, Y. Parkhomenko, *et al.*, *J. Alloys Compd.*, 2022, **912**, 165208.

88 L. Jiang, L. Han, C. Lu, S. Yang, Y. Liu, H. Jiang, Y. Yan, X. Tang and D. Yang, *ACS Appl. Mater. Interfaces*, 2021, **13**, 11977–11984.

89 Y. Lei, R. Zheng, H. Yang, Y. Li, C. Yong, X. Jiang, R. Liu and R. Wan, *Scr. Mater.*, 2021, **199**, 113885.

90 Y.-c. Liu, J.-L. Lan, B. Zhan, J. Ding, Y. Liu, Y.-H. Lin, B. Zhang and C.-w. Nan, *J. Am. Ceram. Soc.*, 2013, **96**, 2710–2713.

91 D. Yang, X. Su, Y. Yan, T. Hu, H. Xie, J. He, C. Uher, M. G. Kanatzidis and X. Tang, *Chem. Mater.*, 2016, **28**, 4628–4640.

92 A. Bhaskar, R.-T. Lai, K.-C. Chang and C.-J. Liu, *Scr. Mater.*, 2017, **134**, 100–104.